Development of a rotary push-cut-type negative-pressure-airflow end-effector for harvesting safflower filaments

Zhenguo Zhang[1,4*], Zhenyu Xing[1,2,3,4], Minyi Zhao[5], Peng Xu[1,4], Quanfeng Guo[1,4], Chao Zeng[1,4], Ruimeng Shi[1,4], Yunze Wang[1,4]

(1. *College of Mechanical and Electrical Engineering, Xinjiang Agricultural University, Urumqi 830052, China*;
2. *Key Laboratory of Modern Agricultural Equipment and Technology (Jiangsu University), Ministry of Education, Zhenjiang 212013, China*;
3. *College of Agricultural Engineering, Jiangsu University, Zhenjiang 212013, China*;
4. *Key Laboratory of Xinjiang Intelligent Agricultural Equipment, Xinjiang Agricultural University, Urumqi 830052, China*;
5. *College of Engineering, Northeast Agricultural University, Harbin 150000, China*)

Abstract: Safflower is one of the most important oil crops worldwide. To improve the efficiency and quality of harvesting soft safflower filaments, minimize filament damage by the blade, and ensure the integrity of the filaments, an end-effector with a rotary push-cut-type negative-pressure airflow was designed. The design of the rotary blade edge curve was based on Archimedean and logarithmic spirals. The effect of the Archimedean spiral on the pushing of the scattered filaments was investigated. The rotary-cutting force and speed of the logarithmic helix on the soft filaments were analyzed. The sliding cut angle and feed speed of the blade are the key factors governing filament removal and damage. A simulation model of the cutting chamber flow field was established for the change in airflow with the position and speed rotation of the blade, allowing analysis of the parameters of the negative-pressure airflow. Single-factor and Box-Behnken tests were performed with the sliding cut angle, blade feed speed, and negative-pressure airflow speed as influencing factors and filament removal, damage, and drop rate as indices. The response surface clarified the effects of various factors on these indices. Optimal parameters were a sliding cut angle of 32.20°, a blade feeding speed of 0.031 m/s, and a negative-pressure airflow speed of 4.57 m/s. The corresponding filament removal, damage, and drop rates were 93.47%, 6.94%, and 4.33%, respectively. Optimization results showed that filament removal, damage, and drop rates were 93.50%, 7.02%, and 4.43%, respectively. The harvesting process met the requirements of high efficiency and low damage.

Keywords: harvesting, safflower filaments, end-effector, rotary push-cut type, negative-pressure airflow
DOI: 10.25165/j.ijabe.20251803.9722

Citation: Zhang Z G, Xing Z Y, Zhao M Y, Xu P, Guo Q F, Zeng C, et al. Development of a rotary push-cut-type negative-pressure-airflow end-effector for harvesting safflower filaments. Int J Agric & Biol Eng, 2025; 18(3): 82–96.

1 Introduction

Safflower is not only an important oil crop but also has applications in various industries including food, cosmetics, dye feed, and pharmaceuticals[1,2]. The worldwide cultivated area of safflower is 8×10^9 m^2, with a production of 6.5×10^7 kg, but manual harvesting is still relied on[3]. Safflower is harvested three to five times after opening, with a short harvesting period and insufficient labor. Large areas of safflower filaments wither when not harvested timely, which affects the opening of the filaments in the next crop. This phenomenon leads to decreased filament production and harvest quality[4,5]. The core component of mechanized harvesting is the end-effector, which directly affects the filament production and quality. The morphology and moisture content of the filaments change gradually after safflower opening. During harvesting, the blade of the end-effector collides with the scattered and soft filaments, potentially leading to fracture, breakage, and extrusion. Some of the fractured filaments do not separate from the fruiting ball, which affects the opening of the subsequent filaments. Harvested filaments remain inside the end-effector, resulting in collisions with mechanical components and damage, even if the extruded filaments and components are stuck together. Subsequent harvesting efficiency and quality are seriously affected, restricting the healthy development of the safflower industry[6-8]. Therefore, optimizing the end-effector to ensure the removal and integrity of filament picking and reduce filament damage has become a technical difficulty in improving the level of mechanized safflower harvesting.

Many studies have been conducted on the structure of end-effectors for rotary cutting and shearing to minimize harvesting crop damage, ensure crop integrity, and improve the removal effect of end-effectors[9-11]. Rotary cutting uses a rotary blade to make one or

Received date: 2025-02-05 **Accepted date:** 2025-04-10
Biographies: Zhenyu Xing, MS, research interest: characteristic crops quality improvement and efficiency technology and intelligent equipment, Email: xingzhenyu151621@163.com; **Minyi Zhao**, MS, research interest: characteristic crops quality improvement and efficiency technology and intelligent equipment, Email: zhao_minyi@126.com; **Peng Xu**, MS, research interest: characteristic crops quality improvement and efficiency technology and intelligent equipment, Email: xupeng9018@163.com; **Quanfeng Guo**, MS, research interest: characteristic crops quality improvement and efficiency technology and intelligent equipment, Email: guoquanfengnl@163.com; **Chao Zeng**, MS, research interest: characteristic crops quality improvement and efficiency technology and intelligent equipment, Email: chaozeng5054@163.com; **Ruimeng Shi**, MS, research interest: characteristic crops quality improvement and efficiency technology and intelligent equipment, Email: 19199276782@163.com; **Yunze Wang**, MS, research interest: characteristic crops quality improvement and efficiency technology and intelligent equipment, Email: Wangyunze_531@163.com.

***Corresponding author: Zhenguo Zhang**, Associate Professor, research interest: characteristic crops quality improvement and efficiency technology and intelligent equipment. College of Mechanical and Electrical Engineering, Xinjiang Agricultural University, No.311, Nongda East Road, Urumqi 830052, China. Tel: +86-15099092586, Email: zhangzhenguo@xjau.edu.cn.

more cuts to the harvested parts[12]. Yin et al.[13] designed a grape-picking device with a grasping and rotary-cut-type underactuated double-fingered hand using a two-finger, four-knuckle hand claw envelope. Acceleration-deceleration trapezoidal control was used to achieve the expansion and contraction of the rotary circular blade and cut off the fruit stalks. Xu et al.[14] developed an orange-harvesting end-effector for a rotary blade using vacuum suction cups to achieve separation. The two-finger gripping mechanism rotates and cuts the orange stalks. Ge et al.[15] proposed a cutting-pneumatic suction method for filament harvesting. A rotary blade was used to cut the roots of the filaments, and the filaments were completely separated from the fruit ball. Filaments were collected by negative-pressure airflow adsorption at a damage rate of 9%. Shear uses two or more blades to cut a separation area[16]. Xiong et al.[17] designed a strawberry harvesting end-effector to segregate other target strawberries using a mechanical finger piece. The swallowed strawberries were cut from the stalks using two sets of oppositely moving blades in chambers. Park et al.[18] proposed a cucumber-harvesting robotic system based on circular saw cutting. Ensuring fast and accurate cutting with a harvesting success rate of 70.8%, a visual servo-guided end-effector directed the pedicel to a point on the circular saw of the cutting module. Wang et al.[19] designed a bite-type citrus-harvesting end-effector. Based on the biting action of snakes and skeletal mouth structure, a linkage mechanism was used to realize the opening and closing of the upper and lower jaws with large opening angles. Different tilting angles of citrus can be realized for envelope biting and fruit stalk shearing. For the end-effector picking design of safflower, Gracia et al.[20] and Manuello et al.[21]proposed the use of cutting-air suction combined harvesting filaments, which improved the harvesting efficiency, but the filament damage rate was high. Cao et al.[22] used comb-tooth cutting to sort out the whole safflower first and then cut and pick it. Although it saved the time of flower picking, the filament picking rate was low. Zhang et al.[23] designed a double-acting pair-cutting end-effector for low-speed shear and segmented operations based on the design idea of low-speed and segmented shear with a damage rate of 5.57%.

Compared with the “cut stalks and separate fruits” of grapes[24], oranges[25], peppers[26], and cucumbers[27], the cutting areas of safflower filaments are soft and scattered. During the filament-cutting process, the cutting speed of the high-speed rotating blade was high, and the effect on gathering scattered filaments was worse. The blade generated a large impact force, which caused filament damage. Although low-speed shear operated at lower speeds, soft filaments with high moisture content were difficult to cut and could disrupt the cutting process. In addition, the unreasonable structure of the filament-cutting chamber and the mismatch of the negative-pressure airflow speed can directly affect filament collection, resulting in filament dropping and damage to the touching wall. Therefore, the design of an end-effector is urgently required to ensure safflower filament removal with high accumulation and low damage.

To address the problems of reduced removal of scattered and soft safflower filaments and serious damage to the filaments, an end-effector with a rotary push-cut-type negative-pressure airflow for safflower filament harvesting was designed. By combining the filament features of the scattered form and soft texture, the blade was designed using Archimedean and logarithmic spirals. Through blade pushing and rotating operations, scattered filaments were gathered to minimize filament damage. An analysis of the filament-cutting process was carried out to build a mechanical model of the blade and filament cutting. A simulation model of the cutting chamber flow field was established for the change in airflow with the position of the rotary blade to determine the parameters of the negative-pressure airflow speed. The motion parameters of the key components of the end-effector were analyzed theoretically. Single-factor and Box-Behnken tests were performed. In future work, the optimized design of the end-effector will be tested in field trials to evaluate its harvesting performance. It is proposed to improve the quality and efficiency of its operations, reduce manual operations, and provide reference for the healthy development of the safflower industry.

2 Materials and methods

2.1 Material features of safflower

The material features of the safflower filaments are the basis for the design of the end-effector[28]. For the selected safflower variety Yunhong No. 6, the material feature parameters were measured in mid-July 2022 at the Yunguang Safflower Cultivation Agricultural Cooperative in Xinjiang, China (Figure 1). The dimensions of the safflower were determined using Vernier calipers and tape measurements. The cutting force at the necking point of the fruit ball was determined by using a TMS-Touch texture tester. In addition, the moisture content of the safflower was determined during the opening period using an electric thermostatic blower-drying oven. The main material parameters of the safflower are listed in Table 1.

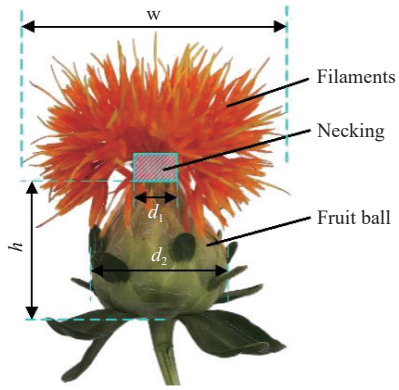

Note: w is the width of filaments, h is the height of fruiting ball, d_1 is the diameter of necking, and d_2 is the diameter of fruiting ball.

Figure 1 Structural diagram of opening safflower

Table 1 Main material feature parameters of safflower

Parameter	Numerical value	Mean value and range
Filaments width/mm	41.94–54.35	50.33±2.88
Necking diameter/mm	2.93–6.97	5.8±0.78
Diameter of fruiting ball/mm	19.62–28.90	25.01±2.30
Height of fruiting ball/mm	17.21–27.43	21.61±2.01
Levitation speeds of filaments/m·s^{-1}	2.03–2.77	2.32±0.45
Moisture content of filaments/%	70.10–80.26	76.56±1.38
Peak cutting force/N	78.86–108.23	90.35±2.57

2.2 Overall structure and working principle

The structure of the safflower filament harvesting robot is shown in Figure 2a. It consists of a rotary push-cut end-effector, filament collection system, filament detection system, central control system, spatial positioning system, and moving system. The rotary push-cut end-effector and safflower detection system were connected to the adjustment platform of the spatial positioning system and flower-collecting system through the filament-conveying hose. The central control system was bolted to the side of

the mobile system. A filament collection system was installed at the bottom of the mobile system. During the operating process, a computer was required for the safflower detection system to provide arithmetic power for data acquisition and obtain the spatial location information of the safflower. Then, the spatial positioning system was adjusted to focus the rotary push-cut end-effector on the filaments for harvesting. Finally, the cut filaments were collected using the filament collection system.

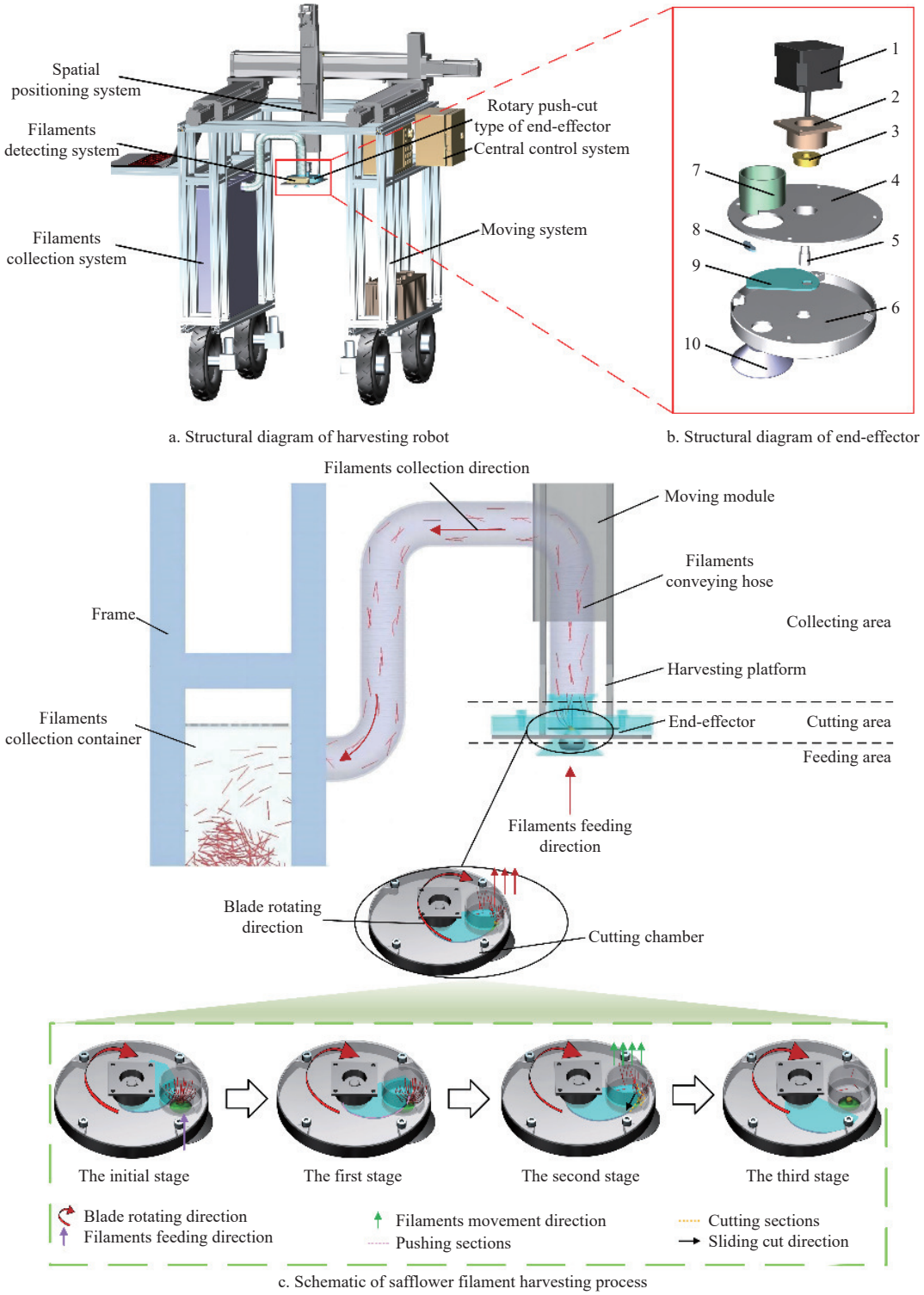

a. Structural diagram of harvesting robot

b. Structural diagram of end-effector

c. Schematic of safflower filament harvesting process

1. Stepping motor 2. Flange 3. Bearing 4. Upper shell 5. Central shaft 6. Below shell 7. Filaments fitting taper 8. Rotary blade 9. Fixed cutter 10. Filament-collecting hose

Figure 2 Rotary push-cut-type safflower-harvesting robot

The rotary push-cut end-effector is one of the most important components of a harvesting robot system[29]. It primarily consists of a stepping motor, an upper shell, a rotary blade, a flower-collecting hose, a filament-fitting taper, and a lower shell, as shown in Figure 2b. Figure 2c shows the three steps of the end-effector cutting process: (i) feeding area, (ii) cutting area, and (iii) collection area. First, the detected filaments enter the filaments that fit the taper in the feeding area. The fruit ball is blocked to the outer side of the filament fitting cone, and the filament is converged into the cutting chamber. The cutting mouth of the end-effector is aligned with the filament. Subsequently, the central control and filament collection systems are activated. The rotary blade pushes and cuts

the safflower necking in the cutting area. Finally, the cut filaments are transported to the filament collection container through a conveying hose in the collection area. During the operating process, when the filaments are fed into the cutting chamber of the end-effector, the stepper motor drives the rotary blade to push the scattered filaments gathered toward the fixed blade, as shown in the first stage of Figure 2c. Then, the rotary blade cooperates with a fixed blade to complete the low-speed supported cutting of the filaments, as shown in the second stage of Figure 2c. The cutting filaments are kept in the cutting chamber to be adsorbed under negative pressure, transported to the filament collection container, and settle under the effects of inertia and gravity, as shown in the third stage of Figure 2c.

2.3 Design of rotary push-cut end-effector

The sliding cut angle and feed speed of the rotary blade affected filament harvesting. The filaments were pushed together before rotary cutting, which minimized the filament damage rate and improved filament removal. Based on the material parameters, the force and speed of the filament sliding cut under the action of the rotary blade were analyzed to determine the key factors affecting filament removal. This provides a theoretical basis for the optimization of structural parameters.

2.3.1 Design of blade edge curve

The blade is the core component of the end-effector. This is also a key component in determining the effect of filament cutting. To achieve better filament removal and minimize filament damage, it is necessary to enhance the cutting action of the blade edge and reduce the cutting-ratio resistance of the filaments[30,31]. Slide cutting is an energy-efficient method[32]. Therefore, slide cutting was used to cut the filaments.

According to the cutting process of the filaments, the blade edge curve was divided into four partitions: the pushing section (Archimedean spiral), sliding cut section (logarithmic spiral), back blade section (straight line), and rotating section (circular line), as shown in Figure 3a. The pushing and sliding sections of the blade edge curve directly affect the pushing and sliding of the filaments. The pushing section contacts the cutting mouth and pushes it toward the fixed blade. The blade edge of the sliding section cooperates with a fixed blade to complete the supported cutting of the filaments.

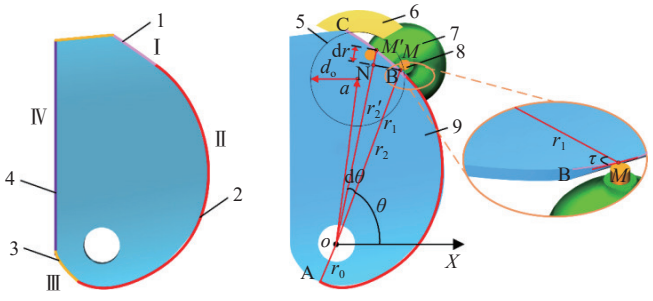

a. Segmentation of blade edge curve b. Sliding cut process of blade edge curve

Note: Ⅰ. Sliding section, Ⅱ. Pushing section, Ⅲ. Rotating section, Ⅳ. Back blade section, 1. Logarithmic spiral, 2. Archimedean spiral, 3. Circular line, 4. Straight line, 5. Filament-cutting mouth, 6. Fixed blade, 7. Fruit ball, 8. Recking, 9. Rotary blade. AB is Archimedean spiral, BC is logarithmic spiral, M is necking mass point, M' is filament-cutting point, r_1 and r_2 are the polar radius of filaments necking mass M, r_2' is the polar radius of vectorial radius r_2 moving to filament-cutting point M', θ is polar angle, dθ is angle by any rotated angle of θ, dr is the increase of vectorial r_2 to r_2', and X is coordinate axis.

Figure 3 Diagram of blade edge curve

To make the filaments at any point in the cutting mouth move toward the fixed blade when in contact with the pushing section, an Archimedean spiral, flaring out equidistantly with the angle of rotation, was chosen as the blade edge curve of the pushing section. The application of Archimedean spiral in blade design has a constant axial truncation preservation and little variation in the back angle, which ensures blade durability[32]. In addition, the Archimedean spiral reduced friction and ensured edge strength. The rotation center of the blade O was considered the origin. The back blade section perpendicular to the blade was considered the X-axis. O-X polar coordination was established for a certain instantaneous plane of the blade, as shown in Figure 3b.

The pushing section of the blade was Archimedean spiral AB. Curvilinear equation was defined as

$$r_1 = r_0 + b\theta \tag{1}$$

$$r_0 = L_o - d_a \tag{2}$$

where, r_1 is the polar radius of Archimedean spiral AB, mm; r_0 is starting polar radius, mm; b is a constant; θ is the angle between the polar radius r_1 and coordinate axis O-X, (°); L_o is the distance between the rotation center of blade O and the center of filament-cutting mouth a, mm; and da is the radius of filament-cutting mouth, mm.

From Equations (1) and (2), the blade edge curve of the pushing section was an Archimedean spiral. According to the difference in the rotation angle θ, different ranges of the rotation angle θ could be selected to obtain different blade edge curves of the pushing section. The machine power consumption and cutting performance of the sliding cut section were directly affected.

The sliding cut force of the blade on the filaments affected the filament removal. According to the sliding cut mechanism of the logarithmic spiral, the blade edge curve of the blade in the sliding cut section was designed with a constant sliding cut angle[33], as shown in Figure 3b. Because of the complexity of the force in the cutting process of filaments, the necking was simplified to be the object of study on the cutting blade as the mass point M. Assuming that the blade was static, the necking mass point M moved along the blade logarithmic spiral BC to the cutting point M'. Therefore, the trajectory of the mass point M was a logarithmic spiral. The necking mass M was cut from the lowest point A of the sliding cut section and slipped along the logarithmic solenoid BC to point B. The polar equation of the logarithmic spiral BC is defined as

$$r_2 = ce^{\theta\cot\tau} \tag{3}$$

where, r_2 is the polar radius of the logarithmic spiral, mm; c is a parameter with the curvature characteristic of the logarithmic spiral, and its value is the distance between the lowermost point A of the logarithmic spiral and the rotation center of the blade O, mm; and τ is the sliding angle of the rotary blade, (°).

When the sliding cut section of the edge curve was turned from any turning angle θ to an angle dθ, the arbitrary necking cutting point M moved along the sliding cut section to the cutting point M', and the vectorial radius r_2 became r_2', thus increasing dr. When dθ is small and tends to 0, arc MM' can be approximated as a straight line. The radius was equal to that of the straight line MM'. According to the definition of the sliding cut angle τ, the tangent equation for the slip-tangent angle τ in $\Delta MM'N$ is given by

$$\tan\tau = \frac{MN}{NM'} = \frac{r_2 \mathrm{d}\theta}{\mathrm{d}r} \tag{4}$$

If the slide tangent angle τ is a constant, such that $\tan\tau = K$ (K is a non-zero constant), then Equation (4) is deformed. Integrating both sides of the equation gives

$$r_2 = ce^{\frac{\theta}{K}} \tag{5}$$

From Equations (3)-(5), the sliding cut section is a logarithmic spiral. The edge curve depended on the edge sliding cut angle τ. According to the current logarithmic spiral curvature feature of research[34], combined with the material properties of safflower, c was set to 55 mm. Different values of the sliding cut angle were substituted into Equation (3) to obtain constant edge curves for different static sliding cut angles. There was a direct impact on filament-cutting harvesting and breakage reduction.

2.3.2 Design of the sliding angle

The sliding cut force of the blade with the sliding angle affects the filament removal and filament damage[35]. With respect to the complexity of the force in the filament-cutting process, reasonably selecting the sliding cut angle could reduce the ratio of resistance of cutting and the cutting damage of filaments. The filament-cutting process was analyzed to simplify the necking as mass C. An analysis of the force and displacement of the filaments is presented in Figure 4.

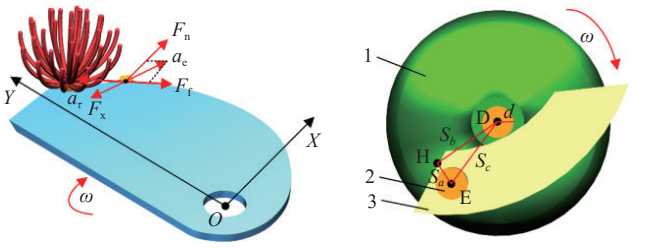

a. Force analysis of filaments b. Displacement analysis of filaments

1. Fruit ball 2. Necking 3. Fixed blade

Figure 4 Force and displacement analysis of filaments

The O-XY coordinate of the blade at a certain instant was established with the center of blade rotation O as the origin. By neglecting the air resistance and incorporating the measured physical and mechanical properties of safflower[36,37], filaments are easily accessible to the cutting mouth. As shown in Figure 4a, if the filament necking mass C was cut by the blade, the mass C would contact the fixed blade, and the fixed blade would play a supporting role. Compared with the force of the blade on the filament, the force of the airflow is minimal and negligible. The force on the mass point C is the normal force F_n of the blade, friction force F_f in the tangential direction of the blade, and friction force F_x. At the instant of filament cutting, the filament necking mass point C rotates rapidly from being static, resulting in a high instantaneous acceleration. Then, the dynamic equation of the mass point C on the cutting surface is directed along the edge curve and blade feed velocity v as follows:

$$\begin{cases} F_n - F_x\cos\tau = ma_e\cos\tau \\ F_x\sin\tau - F_f = ma_\tau - ma_e\sin\tau \\ F_f = F_n\tan\varphi \end{cases} \tag{6}$$

where, φ is the friction angle, (°); m is the average value of individual filament mass, g; a_e is the implicit acceleration of filaments necking mass C, m/s^2; a_τ is the tangential acceleration of filaments necking mass C, m/s^2; F_n is the normal force of filaments necking mass C subjected to the blade, N; F_f is the friction force of filaments necking mass M subjected to tangential force along the blade, N; and F_x is the friction force inside filaments necking mass C, N.

The filament motion is shown in Figure 4b. In ΔDEH, S_a is the critical distance when filament necking is cut off, and its value is equal to the diameter of the fruit ball necking d_1. S_b is the tangential movement distance of the filaments necking along the blade under the action of tangential acceleration, i.e., the sliding cut distance. S_c is the relative distance moved by the filaments necking along the blade. T_1 is the sliding cut time, and its value is equal to the ratio of the relative movement distance of the blade S_c to the forward speed of the machine v_m, meaning that t_1=S_c/v_m. Therefore, the motion–distance equation is as follows:

$$\begin{cases} S_a = d_1 \\ S_b = \dfrac{1}{2}a_\tau t^2 = \dfrac{1}{2}a_\tau\left(\dfrac{S_c}{v_m}\right) = d_1\tan\tau \\ S_c = \dfrac{d_1}{\cos\tau} \end{cases} \tag{7}$$

The average power consumption of the filament-cutting process was composed of the positive pressure and work done by friction.

$$\bar{W} = F_nS_a + F_fS_b + F_xS_c \tag{8}$$

where, $\bar{W}$ is the average power consumption of the filament-cutting process, J.

Combining Equations (6) to (9) gives

$$\bar{W} = \frac{mv_m^2d_1\sin(2\tau)(1+\tan\tau\tan\varphi+\sec^2\tau)}{\tan\tau-\tan\varphi} \tag{9}$$

According to the cutting mechanical properties of the filaments obtained in a previous study[23], Equations (6) to (9) show that the filament removal rate is related to the sliding cut angle τ. According to the literature[38], the sliding cut power consumption must be greater than zero to produce the sliding cut effect. From Equation (9), φ≤τ. However, the sliding cut angle is too large, which leads to an increase in cutting power consumption. The filaments slide along the blade edge, reducing the life of the blade. Therefore, the sliding cut angle should be satisfied with τ≤π/2-φ. Following the previous test[39], the friction angle is measured to be φ=23° between filaments and the blade. Consequently, the range of blade sliding cut angle is 23°-67°.

2.3.3 Design of the blade rotary speeds

The blade feed speed is defined as the distance inside the filament necking that is fed within a certain period. By constructing the mechanics model of blade filament cutting, the key factors affecting filament harvesting were clarified, as shown in Figure 5.

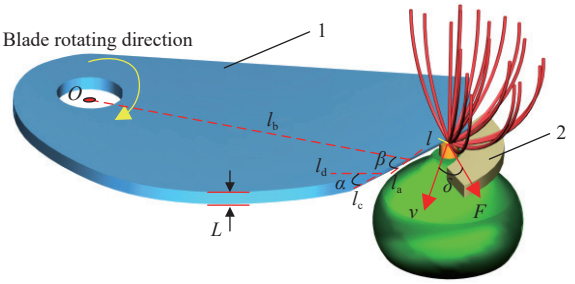

Note: O is the blade center, l is the cutting depth of the blade, l_a is the tangent line of the blade edge, l_b is the line from the cutting point to the center of the circle, l_c is the tilting line of the blade edge, l_d is the horizontal line parallel to the blade, L is the thickness of the blade, δ is the angle between the blade feed speed v and the impact force F, α is the inclination of the blade edge, β is the blade inclination angle, F is the impact force, and v is the blade feed rate.

1. Rotary blade. 2. Fixed blade.

Figure 5 Schematic of blade impact filament

When the sliding cut section of the blade collided with the filaments, it was impacted by the blade. According to momentum quantization,

$$Ft_2 = mv \tag{10}$$

where, F is the impact force of the filaments on the blade, N; t_2 is the cutting time, s; m is the average value of the individual filament mass, g; and v is the blade feed speed, m/s.

Safflower filaments are elastic. When exposed to an impact force, the filaments deform elastically. The contact area of the blade with the filaments increases after the localized deformation of the filaments. The angle is δ between the blade feed rate v and the impact force F. δ is equal to the tilting angle β of the blade. During the cutting of the filaments with the blade, the blade feed rate v is maintained constant.

$$l = vt \tag{11}$$

where, l is the cutting depth of the blade, mm.

Assuming that the impact load acts entirely on the filaments, the critical condition that causes the filaments to fracture is

$$F \geq \sigma_s A \tag{12}$$

where, σ_s is the ultimate stress for filaments to fracture, Pa; A is the filament-cutting area, mm^2.

According to the related literature[40], the blade inclination angle β is equal to the sliding cut angle τ. During the cutting process of the blade on the filaments, v remains constant. By ignoring the curvature of the blade and filament contact surfaces, the area of action during filament cutting is

$$A = 2lL\frac{\tan\frac{\alpha}{2}}{\cos\tau} \tag{13}$$

where, L is the thickness of the rotary blade, mm.

From Equations (11)–(13), it can be obtained

$$v^2 \geq \frac{\sigma_s l^2 L\tan\frac{\alpha}{2}}{m\cos\tau} \tag{14}$$

To satisfy the requirement of filament cutting, the approximate calculation of the ultimate stress is

$$\sigma_s = \frac{F_t}{A_s} \tag{15}$$

where, F_t is the peak cutting force, N; A_s is the sectional area of the filament-cutting, mm^2.

The feed rate of blade v should satisfy the following requirement:

$$v \geq \sqrt{\frac{2\times10^6 F_t l^2 L\tan\frac{\alpha}{2}}{A_s m\cos\tau}} \tag{16}$$

According to previous material feature measurements of safflower, the average value of the individual filament quality m was 1.55×10^{-3} kg. The peak cutting force F_t reached the maximum when the filaments were about to be completely cut off; therefore, l=6.62×10^{-3} m was set. When the filaments were cut by the low-speed support, the maximum peak cutting force $F_{t\,max}$ was 108.23 N, and the cross-sectional area A_s of the filament-cutting was 1.76×10^{-5} m^2. Combining Equations (14)-(16), the component was able to cut off filaments at a blade feed rate v≥9.69×10^{-3} m/s.

As the feed rate of the blade increased, the cutting force for filament cutting decreased. However, when the feed speed of the blade increased, the impact force on the filaments increased, causing filament damage. Combining theoretical analysis and single-factor test, when the blade feeding rate v was 0.02-0.04 m/s, the rate of filament damage was lower and had a better removal effect.

2.4 Cutting chamber of the end-effector

The negative-pressure airflow speed, determined mainly by the air volume and pressure, is an important factor affecting the filament removal and drop rate[41]. To reduce the harvested safflower filaments dropping out of the end-effector and causing rotary-cutting secondary damage, a filament-cutting mouth generates an airspeed that is faster than the suspension speed of the filaments.

2.4.1 Design of negative-pressure airflow

The principles of displacement and terminal speed were used to determine the air volume of the negative-pressure airflow[42,43]. The negative-pressure airflow could suck in all the air contained in the filament-gathering pipe. The airspeed at the filament-cutting mouth cannot be lower than the suspension speed of the filament. According to the principle of displacement, the air volume is the volume between the bottom of the filament-gathering pipe and the sectional area of the filament length, as shown in Figure 6a and 6b.

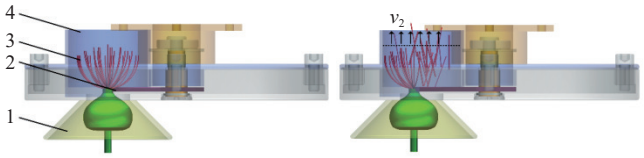

a. Filaments enter the cutting chamber b. Filaments being cut for gathering collection

1. Filaments fitting taper, 2. Rotary blade, 3. Safflower filaments, 4. Filaments gathering pipe, and v_2 is the speed of the airflow to reach the filaments gathering pipe section.

Figure 6 Air displacement way of the end-effector

Ten safflowers were removed from each of the 1-3 d opened filaments. The filaments were placed in a suspension speed-measuring device. The fan speed was varied by adjusting the frequency converter. The airflow speed in the conical observation tube was adjusted. When the filament floated up and down at a certain scale position, it was considered to have reached the desired critical state of levitation. According to the results of the filament suspension speed test in Table 1, v_2 was set to 3.5 m/s for the collection of filaments on different days. Considering the air volume of the leakage and reserve in the collection, the calculated air volume of the fan was 29.4 m^3/s.

The total pressure P generated by the negative-pressure fan is a key factor in the collection efficiency of safflower filaments[41]. The air pressure of the fan consists mainly of the dynamic pressure P_d and static pressure P_s (friction pressure P_m and local pressure P_i). In this case, the dynamic pressure P_d is the dynamic pressure that provides kinetic energy for the movement of airflow inside the chamber and is the main pressure for the fan to realize filament transport. Static pressure P_s is used to overcome the static pressure of the various resistances in the flow. The total pressure P is the sum of the dynamic pressure P_d and static pressure P_s and is calculated as

$$P = P_d + P_m + P_i \tag{17}$$

$$\begin{cases} P_d = \dfrac{1}{2}\rho v_3^2 \\ P_m = \dfrac{\mu}{4R}\dfrac{\rho v_3^2}{2}L_c \\ P_i = \xi\dfrac{\rho v_3^2}{2} \end{cases} \tag{18}$$

where, P, P_d, P_m, and P_i are total pressure, dynamic pressure, friction pressure, and local pressure, respectively (all in Pa); ρ is the air density (1.22 kg/m^3); v_3 is the velocity of the airflow (7 m/s); μ is the friction factor (0.1); R is the radius of the filament-conveying hose (0.05 m); ξ is the local resistance coefficient (1.3); and L_c is the length of the filament-conveying hose (1.2 m).

It was calculated that P_d=7.47 Pa, P_m=4.48 Pa, P_i=9.71 Pa, and P=21.66 Pa. Combined with the safflower filament levitation velocity test, when the airflow velocity $v_2 \geq 3.5$ m/s at the sectional area of filament-gathering tube, the harvested filaments could be sent to the collection container by the negative airflow.

2.4.2 Simulation analysis of the flow field in the cutting chamber

The flow field carried lightweight filaments to reach the filament collection container. The flow field inside the harvesting chamber was analyzed to explore the airflow motion characteristics within the cutting chamber. Consequently, the key factors of the negative-pressure airflow speed affecting filament removal and dropping were determined to provide a theoretical basis for the optimization of the structural parameters.

The chamber structure directly affects the flow field and filament motion. Based on a comprehensive consideration of the filament moisture content, suspension rate, fan energy consumption, and noise, a negative-pressure fan with an adjustable speed was selected. ANSYS18.0/Fluent module was used to set the model boundary conditions. The flow field inside the chamber was simulated and analyzed. The model was simplified according to the simplification principle of numerical analysis and modeling, as shown in Figure 7a. The simplified chamber model[43] was divided into unstructured hexahedral meshes, with 67 286 meshes, 14 296 nodes, and a mesh gap of 3 mm, as shown in Figure 7b.

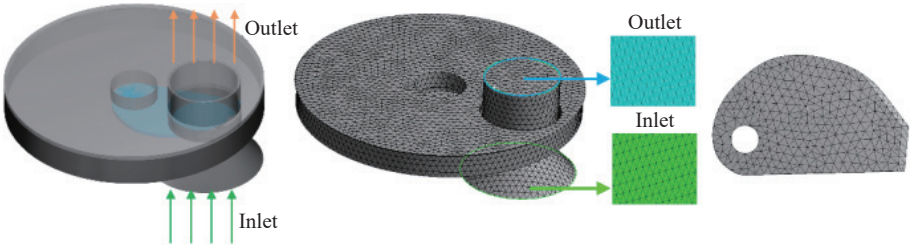

a. Cutting chamber model b. Mesh division results c. Mesh results of blade

Figure 7 Flow field simulation of the cutting chamber

The simulation was used to analyze the distribution of the flow field in the cavity of the end-effector under a change in the negative-pressure airflow speed. Based on the negative-pressure airflow calculations presented in Section 3.2.1 and the actual measurements, an airflow speed of 2-6 m/s was selected for calculation and analysis with a gradient of 1 m/s. The airflow speed at the safflower filament-cutting mouth was varied by adjusting the turbine centrifugal fan, and the turbine centrifugal fan speed was measured. In accordance with a previous study[44], the fan speed n_f is the key parameter of the negative-pressure fan operation, and the relationship between the speed of the fan and the total pressure is

$$n_f = \frac{30}{\pi R_f}\sqrt{\frac{Pg}{\psi\gamma}} \quad (19)$$

where, n_f is the fan speed, r/min; R_f is the radius of the fan impeller, m; γ is the air capacity (11.77 N/m^3); g is the acceleration due to gravity (9.8 m/s^2); and ψ is the pressure coefficient (494).

The pressure inlet was set as the boundary condition of the filament-cutting mouth. Combined with the actual situation, the atmospheric pressure was set as the boundary value, and the pressure was 1.01×10^5 Pa. The pressure outlet was set as the outlet boundary condition. The negative-pressure value was equal to that of the negative-pressure air chamber. Different negative-pressure airflow speeds were realized with a change in the negative-pressure value. According to a previous study[45], the wall boundary condition was rigid with no sliding walls. The initial temperature of the flow field was set to 30°C. At different negative-pressure airflow speeds, the flow field of the rotary cutter for the end-effector was simulated at different pushing and cutting positions. A vector diagram of the velocity distribution of the flow field in the cutting chamber is obtained, as shown in Figure 8.

The blade was placed at the push-together position of the safflower filament, as shown in Figure 8a. When the negative-pressure airflow speed was 2.00 m/s, a large high-speed area was formed between the sliding section of the rotary blade and fixed blade, and the speed of the pushing section was low. As the negative-pressure airflow speed increased, the high-speed area gradually moved from the sliding section to the pushing section. When the negative-pressure airflow speed was 3.00 m/s, the high-speed area was located at the junction of the cut and push sections. The speed distribution of the cutting mouth was uniform. Meanwhile, airflow disturbance occurred in the back blade section, which had no obvious effect on filament gathering. This situation was favorable for the collection of filaments. The high-speed area was transferred to the edge position of the cutting mouth and pushing section at 4.00 m/s. The high-speed area gradually weakened at 5.00 m/s; however, there were multiple vortex phenomena inside the chamber. The airflow disturbances around the cutting mouth and inside the chamber increased significantly by 6.00 m/s. The vortex area increased gradually, which was unfavorable for filament gathering.

The blade was at the sliding cut position of the safflower filament, as shown in Figure 8b. When the negative-pressure airflow speed was 2.00 m/s in Figure 8b, the airflow inside the chamber was disturbed owing to the obstruction of the rotary blade and the fixed blade at the filament-cutting mouth, resulting in the phenomenon of multiple vortices. As the negative-pressure airflow speed was increased to 3.00-5.00 m/s, an airflow disturbance was generated between the two blades, resulting in the formation of a large high-speed area at the pinch angle. The speed of the sliding cut section with the rotary blade was greater than that of the pushing section, which was beneficial for rapid agglomeration and collection of filaments. However, when the negative-pressure airflow speed increased to 6.00 m/s, multiple vortex areas inside the chamber gradually increased, resulting in a small number of filaments remaining.

Combined with the results of the previous test and numerical simulation, when the negative-pressure airflow speed was less than 3.00 m/s, the airflow speed of the chamber was lower, making it unfavorable for filament collection. When the negative-pressure

airflow speed was greater than 5.00 m/s, the flow field inside the chamber was excessively large, resulting in an increased disturbance of the flow field and vortex loss. A comprehensive theoretical analysis and simulation calculations showed that the negative-pressure airflow speed of the safflower filament-cutting port is between 3.00 and 5.00 m/s, which is a more stable flow field in the cavity of the end-effector. This had a positive effect on safflower filament collection.

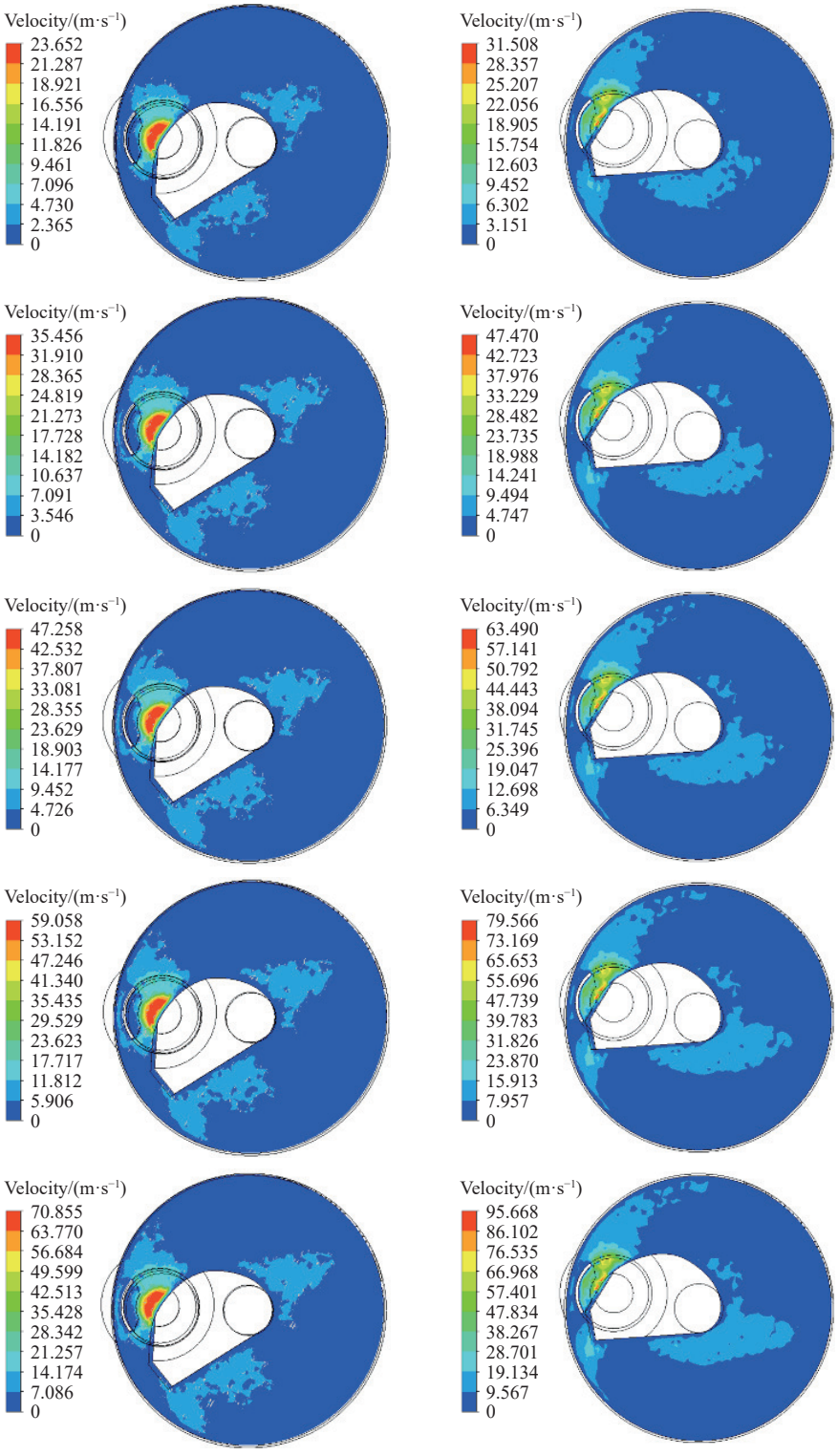

a. The pushing sections of the rotary blade b. The sliding sections of the rotary blade

Figure 8 Cloud diagram of the flow field at the end-effector

3 Tests and results

3.1 Test materials and equipment

A safflower-harvesting test bench was constructed in June 2023 at the Yunguang Safflower Cultivation Agricultural Cooperative in Xinjiang, China. The tested safflower was Yunhong No. 6 grown in Yili, Xinjiang, China. The test equipment was an end-effector with rotary push-cut-type negative-pressure airflow for safflower filament harvesting test bench (homemade by the team), which was mainly composed of an end-effector, a flower collection container,

filament-conveying hose, a power supply, a stepping motor control container, and a vortex blower (Delta BFB1012H, with a speed regulation range of 0.50-6.00 m/s), as shown in Figure 9. The test equipment mainly included Vernier caliper (Wenzhou Maikelen Electric Appliance Co., Ltd., range 0-150 mm, accuracy 0.02 mm), DLY-2301 tachometer (Dexerials Group Co., Ltd., range 2.5-99 999 r/min, accuracy 0.10 r/min), TMS-Touch Mass Tester (Shanghai Tengbao Instrument Technology Co., Ltd., range 0-2500 N, precision 0.01 N).

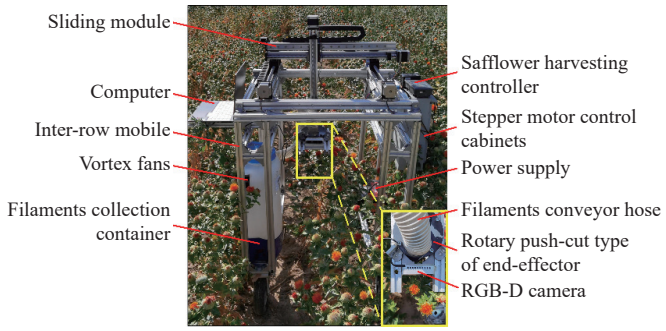

Figure 9 End-effector with rotary push-cut type of negative-pressure airflow for safflower filament harvesting test bench

3.2 Single-factor test

Based on the analysis in Sections 2.3 and 2.4, combined with the structure and working parameters of the end-effector with a rotary push-cut-type negative-pressure airflow for safflower filament harvesting, the test selected three key factors affecting the harvesting effect: the blade sliding cutting angle x_1, blade feeding speed x_2, and negative-pressure airflow speed x_3. The single-factor test was conducted with the safflower filament removal rate y_1, safflower filament damage rate y_2, and safflower filament drop rate y_3 as evaluation indices of the harvesting effect. According to GB/T 5262-2008 "General Provisions on Methods for Determining Test Conditions of Agricultural Machinery," a total of 1200 safflowers that opened for 1-3 d were randomly cut as samples in multiple batches, taking the average of three tests as the results. The formula for calculating each index is given by Equations (20)-(22).

The percentage of the filaments removed from a single fruit ball relative to the total filaments is the filament removal rate, calculated using the following equation:

$$y_1 = \frac{m_1 + m_2}{m_1 + m_2 + m_3} \times 100\% \quad (20)$$

where, y_1 is the filament removal rate, %; m_1 is the quality of filaments picked from the single fruit ball and collected in the filament collection container, g; m_2 is the quality of filaments picked from the single fruit ball and dropped out of the end-effector, g; and m_3 is the quality of unpicked filaments on the fruit ball, g.

The percentage of broken and shattered (broken filaments: a condition in which the filaments or roots have been cut off; shattered filaments: a condition in which the filaments have been cut off into pieces) harvested filaments on a single fruiting ball relative to the picked filaments is the filament damage rate, calculated using the following equation:

$$y_2 = \frac{m_4}{m_1 + m_2} \times 100\% \quad (21)$$

where, y_2 is the filament damage rate, %; m_4 is the quality of the broken filaments in the harvested filaments, g.

The percentage of the harvested filaments on a single fruiting ball that remain and fall out of the end-effector and hose (including cut, natural, and machine drops) relative to the harvested filaments is the filament drop rate[22,46], calculated using the following equation:

$$y_3 = \frac{m_2}{m_1 + m_2} \times 100\% \quad (22)$$

where, y_3 is the filament drop rate, %.

3.3 Box-Behnken test

A response surface design experiment was adopted to analyze the effects of different blade sliding cut angles x_1, blade feed speed x_2, and negative-pressure airflow speed x_3 of the end-effector on the mechanical operational performance of safflower harvesting and to obtain the optimal working parameter combination. The Box-Behnken central composite design principle was used. Three factors and three levels were designed based on a one-factor test, conducting a Box-Behnken central composite test[47]. The test factors and their levels are listed in Table 2.

Table 2 Factor codes of response surface test

Level	Sliding cut angle x_1/(°)	Blade feed speed x_2/(m·s^{-1})	Negative-pressure airflow speed x_3/(m·s^{-1})
–1	23	0.02	3.00
0	45	0.03	4.00
1	67	0.04	5.00

3.4 Results and discussion of the single-factor test

At a blade feed speed of 0.03 m/s and negative-pressure airflow speed of 4.00 m/s, the sliding cut angles of the blade were selected to be 1°, 23°, 45°, 67°, and 89° for the single-factor test. Figure 10a shows that the removal rate was maintained above 92% and first increased and then decreased with a change in running speed. With increasing running speed, the damage rate decreased and the drop rate increased gradually. Therefore, a larger sliding cut angle can improve the effect of the blade sliding cut, reduce the normal pressure at the blade edge, and minimize filament damage. However, when the sliding cut angle was excessively large, the friction power consumption increased significantly. According to previous tests and theoretical analyses, the sliding cut angle was selected to be 23°–67°.

At a sliding cut angle of 45° and a negative-pressure airflow speed of 4.00 m/s, the blade feed speeds were selected to be 0.01, 0.02, 0.03, 0.04, and 0.05 m/s for the single-factor test. Figure 10b shows that the removal rate first increases and then decreases, and the breakage rate gradually increases with increasing blade feed speed. The removal rate was highest when the blade feed speed was 0.03 m/s. When the blade feed speed was 0.05 m/s, the damage rate reached 6.87%. In this case, the blade feed speed was extremely high, causing a large air disturbance, which could easily lead to filament damage. Therefore, when the cutting speed v was 0.02-0.04 m/s, it had a better harvesting effect. The central level was set at 0.03 m/s, and the upper and lower levels were 0.02 m/s and 0.04 m/s, respectively.

At a blade feed speed of 0.03 m/s and a sliding cut angle of 45°, the negative-pressure airflow speed was selected to be 2.00, 3.00, 4.00, 5.00, and 6.00 m/s for the single-factor test. Figure 10c shows that the filament drop rate reached 4.92% at the negative-pressure airflow speed of 4.00 m/s. With an increase in negative-pressure airflow speed, the filament drop rate decreased gradually, reaching 4.12%. Therefore, if the negative-pressure airflow speed is too low, the filaments can easily remain in the chamber of the harvesting robot. The loss of filaments resulted in worse quality of harvested filaments. Based on previous tests, the negative-pressure airflow speed was selected to be 3.50-5.50 m/s.

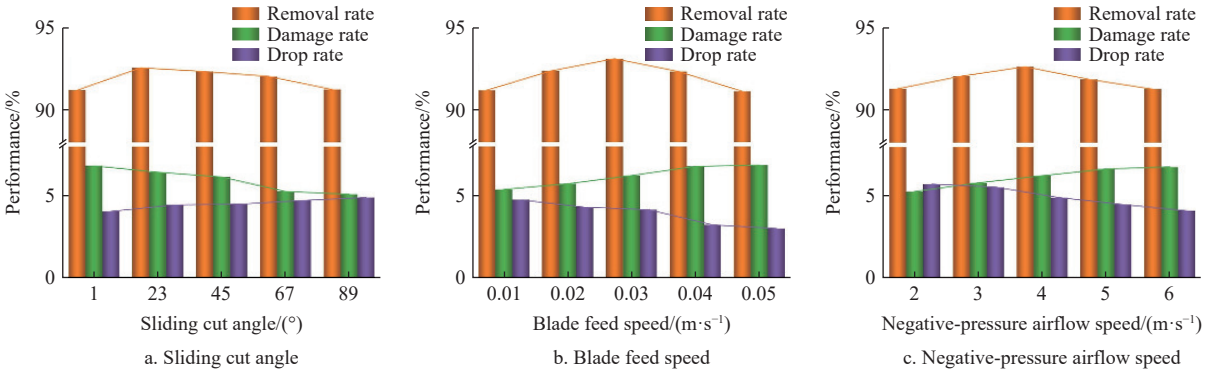

a. Sliding cut angle b. Blade feed speed c. Negative-pressure airflow speed

Figure 10 Effect of single factor on filament harvesting performance

3.5 Results and discussion of the Box-Behnken test

The test program and results are presented in Table 3, with a total of 17 test groups. These included 12 analytical factors and five null estimation errors, with Groups 1-12 being the analytic factor design tests and Groups 13-17 the central design tests[48].

Table 3 Test results of Box-Behnken

Number	Sliding cut angle of blade/(°)	Blade feed speed/(m·s⁻¹)	Negative-pressure airflow speed/(m·s⁻¹)	Removal rate y_1/%	Damage rate y_2/%	Drop rate y_3/%
1	23	0.02	4.00	91.02	8.30	5.29
2	67	0.02	4.00	87.78	6.54	6.44
3	23	0.04	4.00	92.16	8.69	5.32
4	67	0.04	4.00	91.61	9.25	6.18
5	23	0.03	3.00	90.67	7.21	7.06
6	67	0.03	3.00	90.88	7.96	6.47
7	23	0.03	5.00	93.45	7.42	4.84
8	67	0.03	5.00	90.47	6.41	5.07
9	45	0.02	3.00	87.79	6.84	4.31
10	45	0.04	3.00	88.58	7.54	7.28
11	45	0.02	5.00	88.65	5.77	5.60
12	45	0.04	5.00	93.07	7.91	4.06
13	45	0.03	4.00	92.16	6.38	4.85
14	45	0.03	4.00	92.21	6.67	4.56
15	45	0.03	4.00	92.05	6.49	4.83
16	45	0.03	4.00	92.53	6.18	4.03
17	45	0.03	4.00	92.80	6.71	4.35

3.5.1 Regression modeling and significance tests

By analyzing the variance using Design-Expert, the coded regression mathematical model of the filament removal rate y_1, filament damage rate y_2, and drop rate y_3 on the sliding cut angle x_1, blade feed speed x_2, and negative-pressure airflow speed x_3 were established.

The results of variance analysis are presented in Table 4. From the variance analysis of the filament removal rate y_1, the order of the primary and secondary effects of the factors and factor interactions was x_2^2, x_2, x_3, x_1, x_3^2, $x_2\,x_3$, $x_1\,x_3$, $x_1\,x_2$, and x_1^2 on the removal rate; the effects of x_1, x_2, x_3, $x_2\,x_3$, x_2^2, and x_3^2 were highly significant ($p < 0.01$), the effects of $x_1\,x_2$ and $x_1\,x_3$ were significant ($0.01 \le p < 0.05$), and x_1^2 was not significant ($p > 0.05$).

From the variance analysis of the filament damage rate y_2, the order of the primary and secondary effects of the factors and factor interactions was x_2, x_1^2, x_2^2, $x_1\,x_2$, $x_1\,x_3$, x_3, $x_2\,x_3$, x_1, and x_3^2 on the damage rate; the effects of x_2, $x_1\,x_2$, $x_1\,x_3$, x_1^2, and x_2^2 were highly significant ($p < 0.01$), the effects of x_3 and $x_2\,x_3$ were significant ($0.01 \le p < 0.05$), and x_1 and x_3^2 were not significant ($p > 0.05$).

Table 4 Variance analysis of experimental results

Test index	Removal rate y_1/%		Damage rate y_2/%		Drop rate y_3/%	
	F value	p-value	F value	p-value	F value	p-value
Model	24.98	0.0002	31.39	< 0.0001	6.18	0.0127
x_1	23.13	0.0019	5.20	0.0567	1.27	0.2973
x_2	55.70	0.0001	85.99	< 0.0001	0.6705	0.4398
x_3	32.03	0.0008	10.14	0.0154	14.34	0.0068
x_1-x_2	7.78	0.0269	26.24	0.0014	0.0783	0.7877
x_1-x_3	10.94	0.0130	15.10	0.0060	0.6262	0.4547
x_2-x_3	14.17	0.0070	10.11	0.0155	18.94	0.0033
x_1^2	0.0856	0.7784	77.56	< 0.0001	13.15	0.0084
x_2^2	57.12	0.0001	44.59	0.0003	2.12	0.1883
x_3^2	20.01	0.0029	3.55	0.1015	2.77	0.1398
Lack-of-fit	4.37	0.0941	1.20	0.4165	3.94	0.1094

Note: highly significant ($p < 0.01$), significant ($0.01 \le p < 0.05$).

From the variance analysis of the filament drop rate y_3, the order of the primary and secondary effects of the factors and factor interactions was $x_2\,x_3$, x_3, x_1^2, x_3^2, x_2^2, x_1, x_2, $x_1\,x_3$, and $x_1\,x_2$ on the drop rate; the effects of x_3, $x_2\,x_3$, and x_1^2 were highly significant ($p < 0.01$), and x_1, x_2, $x_1\,x_2$, $x_1\,x_3$, x_2^2, and x_3^2 were not significant ($p > 0.05$).

For the lack-of-fit, the p-values of the regression model for the removal rate y_1, damage rate y_2, and drop rate y_3 were all greater than 0.05; therefore, they were not significant. This indicated that the regression model was not a misfit. After removing the insignificant factors, the regression models for the removal rate y_1, damage rate y_2, and drop rate y_3 were obtained, as shown in Equations (23)-(25).

$$y_1 = 92.35 - 0.82x_1 + 1.27x_2 + 0.97x_3 + 0.67x_1x_2 - 0.80x_1x_3 + 0.91x_2x_3 - 1.78x_2^2 - 1.05x_3^2 \quad (23)$$

$$y_2 = 6.49 + 0.74x_2 - 0.26x_3 + 0.58x_1x_2 - 0.44x_1x_3 + 0.36x_2x_3 + 0.97x_1^2 + 0.74x_2^2 \quad (24)$$

$$y_3 = 4.52 - 0.69x_3 - 1.13x_2x_3 + 0.92x_1^2 \quad (25)$$

Based on the analysis of the F value for each factor in Table 4, the factors affecting the filament removal rate were the blade feed speed, negative-pressure airflow speed, and sliding cut angle, in descending order. The factors affecting the filament damage rate were blade feed speed, negative-pressure airflow speed, and sliding cut angle, in descending order. The factors affecting the filament drop rate were negative-pressure airflow speed, sliding cut angle, and blade feed speed, in descending order.

3.5.2 Response analysis of test factors

(1) Effect of interaction term on filament removal rate

When the negative-pressure airflow speed was fixed at 0 level (x_3=4.00 m/s), the effect of the interaction between the sliding cut angle and blade feed speed on the filament removal rate is shown in Figure 11a. For a blade feed speed less than 0.032 m/s, the filament removal rate increased gradually with an increase in the blade feed speed and a decrease in the sliding cut angle. However, for blade feed speeds greater than 0.032 m/s, the filament removal rate decreased with increasing blade feed speed and blade sliding angle. With increasing blade feed speed and sliding cut angle, the force of the blade on the filament increased. It was easier to separate the filaments from the fruit balls.

When the blade feed rate was fixed at 0 level (x_2=0.03 m/s), the effect of the interaction between the sliding cut angle and the negative-pressure airflow speed on the filament removal rate is shown in Figure 11b. For a sliding cut angle less than 28°, the filament removal rate increased with the increase of negative-pressure airflow speed. When the negative-pressure airflow speed was fixed, the filament removal rate decreased with an increase in the sliding cut angle. Because the sliding cutting angle was too large, the sliding cutting effect was not evident, resulting in safflower filaments that were not easily separated from the fruit ball.

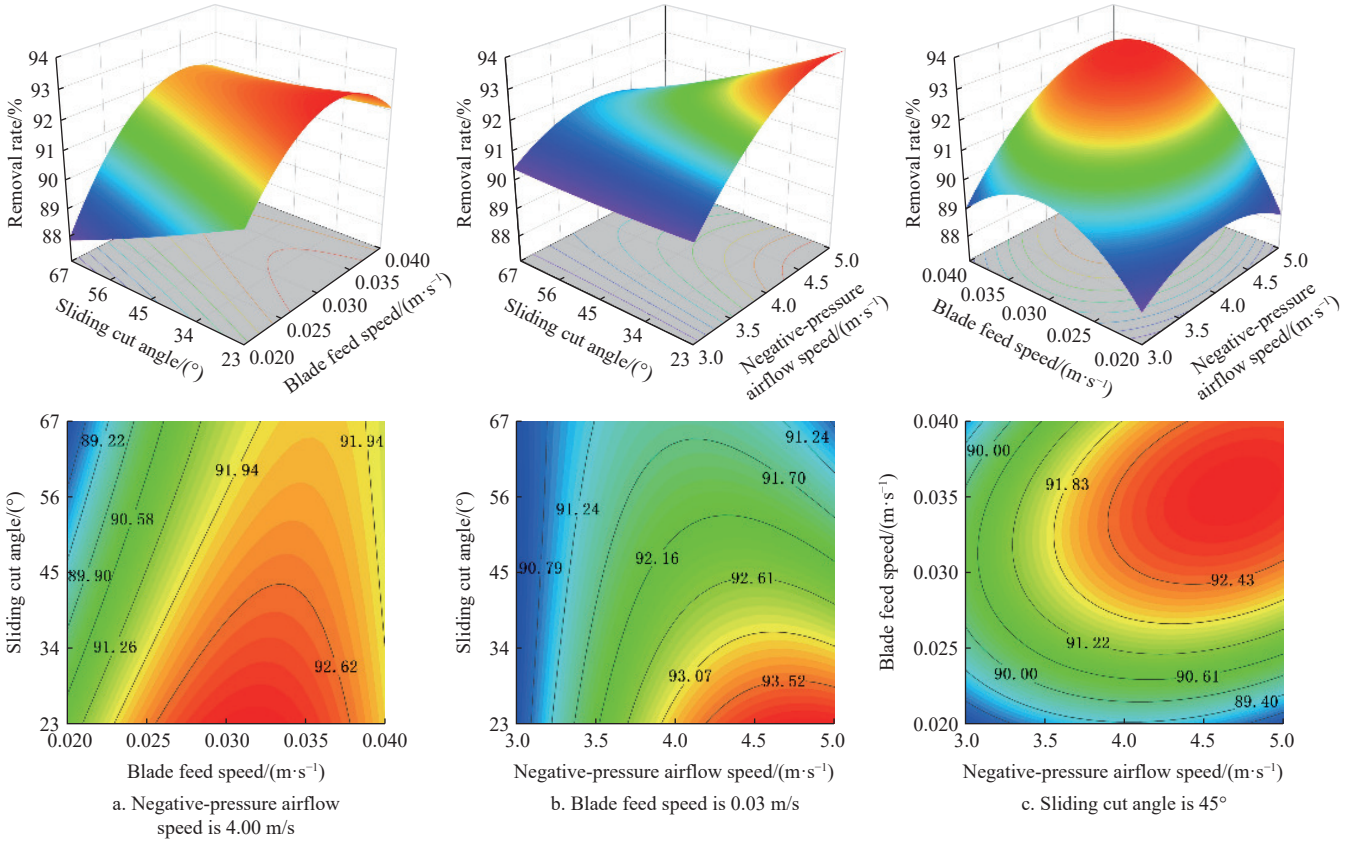

a. Negative-pressure airflow speed is 4.00 m/s

b. Blade feed speed is 0.03 m/s

c. Sliding cut angle is 45°

Figure 11 Effect of interaction on filament removal rate

When the sliding cut angle was fixed at 0 level (x_1=45°), the effect of the interaction between the blade feed speed and the negative-pressure airflow speed on the filament removal rate is shown in Figure 11c. When the negative-pressure airflow speed was less than 4.40 m/s, the filament removal rate initially increased and then decreased with increasing blade feed rate. However, for a negative-pressure airflow speed greater than 4.40 m/s, the filament removal rate increased gradually with an increase in the blade feed speed. In addition, when the blade feed speed was fixed, the filament removal rate increased with sliding cut angle. When the blade feed speed was less than 0.031 m/s, the filament removal rate first increased and then decreased with an increase in the negative-pressure airflow speed. However, for a blade feed speed greater than 0.031 m/s, the filament removal rate increased with an increase in the negative-pressure airflow speed.

The variation of the response surface in Figure 11 shows that the blade feed speed has a significantly greater effect on the filament removal rate than the negative-pressure airflow speed and the sliding cut angle. This was consistent with the results of the ANOVA. Therefore, the final optimized values of the blade feed speed and negative-pressure airflow speed should be as large as possible within the range of the experiment values and the sliding cut angle as small as possible to achieve a higher filament removal rate.

(2) Effect of interaction term on filament damage rate

When the negative-pressure airflow speed was fixed at 0 level (x_3=4.00 m/s), the effect of the interaction between the sliding cut angle and blade feed speed on the filament damage rate is shown in Figure 12a. For a sliding cut angle less than 29°, filament damage first decreased and then increased with the decrease of the blade feed speed. However, for a sliding cut angle of more than 29°, the filament damage rate gradually decreased with a decrease in the blade feed speed. In addition, when the blade feed speed was fixed, the filament damage rate initially decreased and then increased with an increase in the sliding cut angle, and the increasing trend gradually slowed. As the blade feed speed was lower, the peak cutting force of the filaments increased; thus, the effect of the blade was greater on the broken filaments. By contrast, the impact of the blade on the filaments increases, resulting in filament damage.

When the blade feed speed was fixed at 0 level (x_2=0.03 m/s),

the effect of the interaction between the sliding cut angle and the negative-pressure airflow speed on the filament damage rate is shown in Figure 12b. The filament damage rate first decreased and then increased with changes in the sliding cut angle and negative-pressure airflow speed. For the sliding cut angles greater than 26°, the filament damage rate decreased with an increase in negative-pressure airflow speed. However, for a sliding cut angle less than 26°, the filament damage rate increased with the increase of negative-pressure airflow speed. In addition, when the negative-pressure airflow speed was fixed, the filament damage rate initially decreased and then increased with an increase in the sliding cut angle. With an increase in the filament sliding distance along the cutting edge of the blade, the sliding cut effect was enhanced when the sliding cut angle was too high; thus, the contact distance between the blade and filaments increased, leading to crushing. In contrast, it causes extrusion and adhesion of the blade and filaments.

When the sliding cut angle was fixed at 0 level (x_1=45°), the effect of the interaction between the blade feed speed and the negative-pressure airflow speed on the filament damage rate is shown in Figure 12c. For a negative-pressure airflow speed of less than 4.00 m/s, the filament damage first decreased and then increased with increasing blade feed speed. However, for negative-pressure airflow speeds more than 4.00 m/s, the filament damage rate increased gradually with an increase in the blade feed speed. In addition, for blade feed speeds less than 0.033 m/s, the filament damage rate decreased with an increase in the negative-pressure airflow speed. However, for blade feed speeds greater than 0.033 m/s, the filament damage rate increased with the negative-pressure airflow speed. When the blade feed speed was too high, the blade impact force was too large, and extrusion was easily produced, resulting in filament damage.

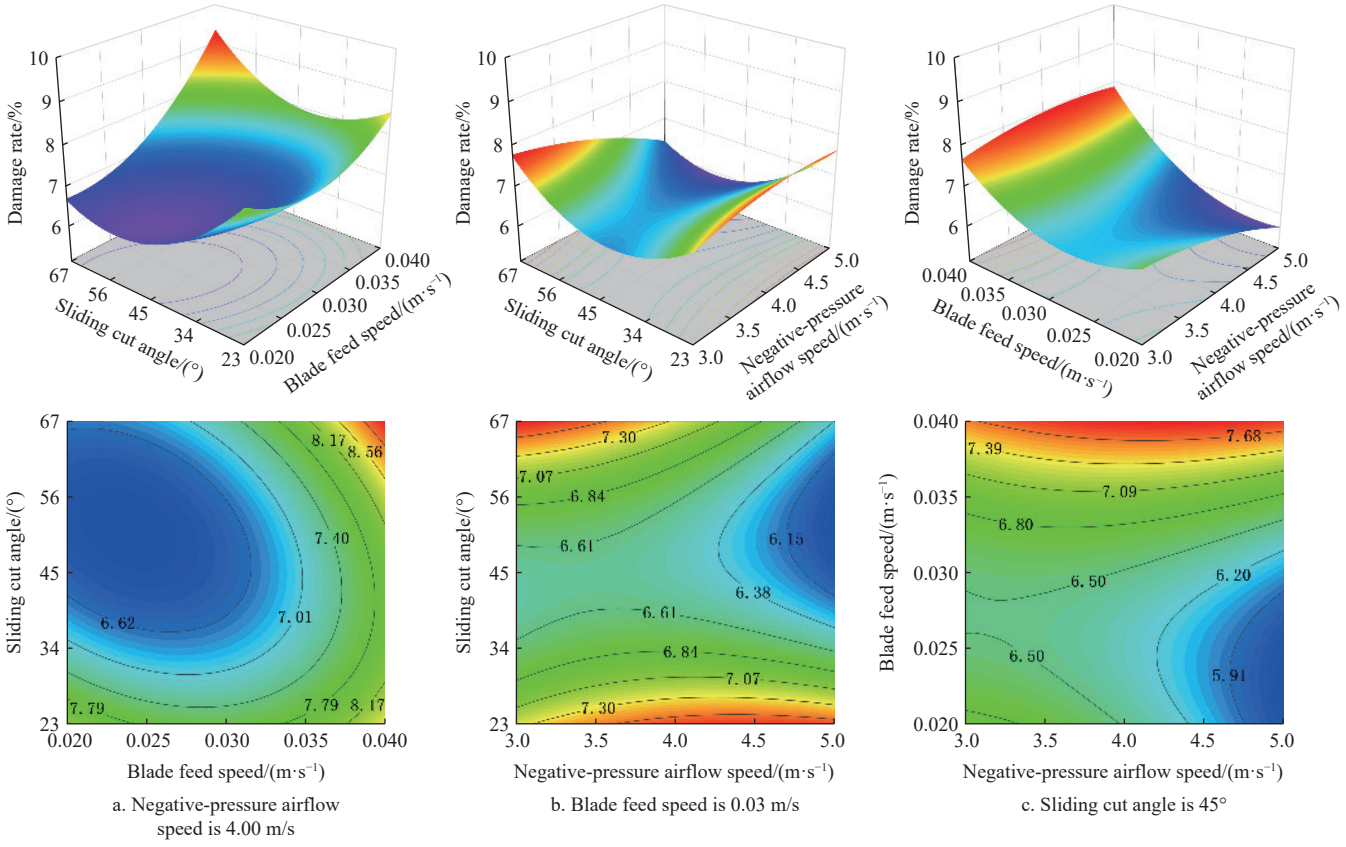

a. Negative-pressure airflow speed is 4.00 m/s

b. Blade feed speed is 0.03 m/s

c. Sliding cut angle is 45°

Figure 12 Effect of interaction on filament damage rate

The variation of the response surface in Figure 12 shows that the blade feed speed has a significantly greater effect on the filament damage rate than the negative-pressure airflow speed and the sliding cut angle. This was consistent with the results of the ANOVA. Therefore, the final optimized values of the negative-pressure airflow speed and sliding cut angle should be as large as possible within the range of the experiment values and the blade feed speed as small as possible to achieve a lower filament damage rate.

(3) Effect of interaction term on the filament drop rate

When the sliding cut angle was fixed at 0 level (x_1=45°), the effect of the interaction between the blade feed speed and the negative-pressure airflow speed on the filament drop rate is shown in Figure 13. For a negative-pressure airflow speed of less than 4.00 m/s, the filament drop rate increased gradually with increasing blade feed speed. However, for negative-pressure airflow speeds more than 4.00 m/s, the filament drop rate decreased gradually with an increase in the blade feed speed. In addition, for the blade feed speed less than 0.03 m/s, the filament drop rate first decreased and then increased with the increase of the negative-pressure airflow speed, and the trend of increase was gradually slower. However, for blade feed speeds more than 0.03 m/s, the filament drop rate decreased with increasing negative-pressure airflow speed. This was mainly because the blade disturbed the flow of the cutting chamber when the blade feed speed was too high, resulting in filament stagnation. Meanwhile, because the negative-pressure airflow speed was too low, the suspension force of the filament was insufficient; thus, the filaments fell off significantly. Figure 13 shows that the filament removal rate varies with blade feed speed and negative-pressure airflow speed.

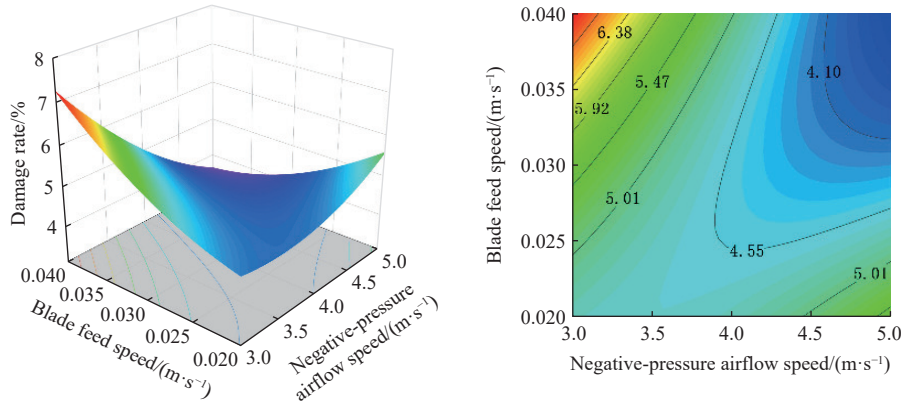

Figure 13 Effect of interaction on filament drop rate

The variation of the response surface in Figure 13 shows that the blade feed speed has a significantly greater effect on the filament drop rate than the negative-pressure airflow speed and the sliding cut angle. This was consistent with the results of the ANOVA. Therefore, the final optimized values of the negative-pressure airflow speed and blade feed speed should be as large as possible within the range of the experiment values to achieve a lower filament drop rate.

3.5.3 Optimization analysis

To ensure better working performance of the end-effector with a rotary push-cut-type negative-pressure airflow for safflower filament harvesting, this study optimized the structure and working parameters of the harvesting device with the harvesting objectives of high removal rate, low breakage rate, and low drop rate. Optimization was performed using Design-Expert[49]. The objective function and constraints are as follows:

$$\begin{cases} \max y_1(x_1, x_2, x_3) \\ \min y_2(x_1, x_2, x_3) \\ \min y_3(x_1, x_2, x_3) \\ 23 \le x_1 \le 67 \\ 0.02 \le x_2 \le 0.04 \\ 3 \le x_3 \le 5 \end{cases} \tag{26}$$

Based on the appropriate model selection, the highest filament removal rate y_1, the lowest damage rate y_2, and the lowest drop rate y_3 were targeted for optimization. When the sliding cut angle was 32.20°, the blade feed speed was 0.031 m/s, and the negative-pressure airflow speed was 4.57 m/s, the safflower was harvested optimally. In this case, the model predicted a removal rate of 93.47%, a damage rate of 6.94%, and a drop rate of 4.33%.

3.6 Field experiments

The field test was conducted from July 20 to July 30, 2023, at the Yunguang Safflower Cultivation Agricultural Cooperative in Xinjiang, China. The operating conditions were the same as those used in the previous tests, and the test conditions and methods were the same as those used in the aforementioned tests[50], as shown in Figure 14a. The test was conducted with a sliding cut angle of 32.20°, a blade feed speed of 0.031 m/s, and a negative-pressure airflow speed of 4.57 m/s. With the relatively slow traction speed (0.20 m/s) of the robot and wait of 25.00-30.00 s after detecting the target filaments, the single cycle time of harvesting was 22.30 s on average for each harvesting process. To eliminate random errors, the test was repeated five times for each parameter combination, as shown in Figure 14b. The results were averaged and showed a removal rate of 93.50%, a damage rate of 7.02%, and a drop rate of 4.43%. The relative errors with the theoretical optimized values were 0.03, 1.14, and 2.26%, and none of the relative errors exceeded 5%. The theoretical values were similar to the experimental values, thereby verifying the accuracy of the model. The operating effects of the machine are shown in Figures 14c and 14d.

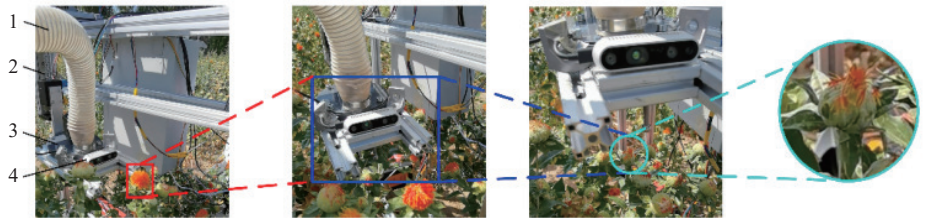

a. Initial state of end-effector b. Harvesting filaments c. Complete harvesting d. Result of harvesting

1. Filament-conveying hose 2. Moving module 3. Rotary push-cut end-effector 4. RGB-D camera

Figure 14 Process and results of the field test

4 Discussion

Different from direct or opposite cutting[51], this paper proposes a new theoretical method of rotary push-cut for multiple stubble plants. Meanwhile, a new blade design method combining Archimedean spiral and logarithmic spiral is adopted. This method rotates and cuts complete filaments at one time by pushing together and collecting scattered filaments. Compared with the pre-designed cutting device research of the group[23,39], the damage rate of the rotary push-cut-type blade is lower than the arc-progressive type by 2.78% and higher than the double-acting opposite direction cutting type by 1.45%. However, the rotary push-cut-type blade has a relatively high removal rate and a significantly higher harvesting effect. It not only ensures the integrity of filaments, but also

effectively reduces the damage of direct or opposite cutting to filaments, and avoids the ineffective growth of subsequent filaments.

Meanwhile, the rotary push-cut-type negative-pressure-airflow end-effector has been demonstrated and promoted in Yunguang Safflower Cultivation Agricultural Cooperative in Xinjiang, China, with remarkable harvesting effect. It has improved the harvesting efficiency and quality of the farmers, which is highly recognized by the local farmers and the president. In addition, accurate positioning of filament harvesting is the focus for reducing breakage and guaranteeing the medicinal properties of safflower. High-efficiency and low-damage filaments are likewise recognized by herbal medicine purchasers. The quality of filaments is better than those harvested by hand or other devices. The next step will be to further upgrade the intelligence and automation, and expand the promotion area to promote the development of the safflower harvesting industry.

It is worth noting that because many plants, such as tea and safflower, are similar, they are also multi-harvested[52]. The actual field working environment and planting mode are also relatively complex and changeable, which limits the development of mechanical harvesting equipment[53,54]. Therefore, the research in this paper can be used as a reference for multi-harvest crops. The harvesting method of safflower is related to the growth feature of multiple crops. This study provides important insights and valuable theoretical methods for solving this problem. The combination of robotic harvesting with autonomous detection and agronomic improvement is considered to be an important direction for future development.

In addition, the design of this device has also significantly influenced the design of mechanization in harvesting fields such as garlic root cutting, peony picking, and rose picking. Therefore, the rotary push-cut-type negative-pressure-airflow end-effector not only improves the efficiency and quality of harvesting, but also provides the basis and reference for the development of the field of agricultural mechanized harvesting.

5 Conclusions

To solve the problems of fractured, broken, and extruded safflower filaments during harvesting, a rotary push-cut end-effector with negative-pressure airflow for safflower filament harvesting was designed. Through theoretical analyses and calculations, the parameters of the key components of the end-effector were estimated. The flow field and structural parameters of the cutting chamber were simulated and analyzed, and the interaction between the end-effector structure and filaments was investigated. The main conclusions are as follows:

(1) Based on Archimedean and logarithmic spirals, a blade was designed to optimize the flow field in the cutting chamber. The separation of filaments and fruit balls can reduce the specific resistance of filament cutting, effectively improve the removal rate of filaments, and decrease cutting damage to the filaments. The sliding cut angle was designed to be 23°–67°, the blade feed speed to be 0.02–0.04 m/s, and the negative-pressure airflow speed to be 3.00–5.00 m/s. The design results can be used as a reference for the structural improvement of the end-effector and optimization of the working parameters.

(2) Single-factor and Box-Behnken tests were performed on a self-constructed platform. The response surface method was used to optimize the test results. The optimal parameters in the validation test were as follows: the sliding cut angle of the blade was 32.20°, the blade feed speed was 0.031 m/s, and the negative-pressure airflow speed was 4.57 m/s. In this case, the model predicted a removal rate of 93.47%, a damage rate of 6.94%, and a drop rate of 4.33%.

(3) An end-effector harvesting test was performed under optimal conditions. The results showed that the removal rate was 93.50%, the damage rate was 7.02%, the drop rate was 4.43%, and the relative errors in the predicted values were not more than 5%. The measured and predicted values of each index were relatively consistent, indicating that the results of parameter optimization were reliable.

Acknowledgements

This research was funded by Central Guidance for Local Science and Technology Development Funding Projects under Grant, China (Grant No. ZYYD2025ZY11), the National Natural Science Foundation of China (Grant Nos. 32460449 and 52265041), the Key Laboratory of Modern Agricultural Equipment and Technology (Jiangsu University), Ministry of Education, China (Grant No. MAET202305), and the Graduate School-level Research and Innovation Program of Xinjiang Agricultural University, China (Grant No. XJAUGRI2023021).

[References]

[1] Zanetti F, Angelini L G, Berzuini S, Foschi L, Clemente C, Ferioli F, et al. Safflower (*Carthamus tinctorius* L.) a winter multipurpose oilseed crop for the Mediterranean region: Lesson learnt from on-farm trials. Industrial Crops and Products, 2022; 184: 115042.

[2] Zhang Z G, Zeng C, Xing Z Y, Xu P, Guo Q F, Shi R M, Wang Y Z. Discrete element modeling and parameter calibration of safflower biomechanical properties. Int J Agric & Biol Eng, 2024; 17(2): 37–42.

[3] Guo H, Luo D, Gao G, Wu T L, Diao H W. Design and experiment of a safflower picking robot based on a parallel manipulator. Engenharia Agrícola, 2022; 42: e20210129.

[4] De Oliveira Neto S S, Zeffa D M, Freiria G H, Zoz T, da Silva C J, Zanotto M D, et al. Adaptability and Stability of Safflower Genotypes for Oil Production. Plants, 2022; 11: 708.

[5] Gongora B, de Souza SN M, Bassegio D, Santos R F, Siqueira J A C, Bariccatti R A, et al. Comparison of emissions and engine performance of safflower and commercial biodiesels. Industrial Crops and Products, 2022; 179: 114680.

[6] Bac C W, Roorda T, Reshef R, Berman S, Hemming J, Van Henten J E. Analysis of a motion planning problem for sweet-pepper harvesting in a dense obstacle environment. Biosystems Engineering, 2016; 146: 85–97.

[7] Barth R, Hemming J, Van Henten E J. Angle estimation between plant parts for grasp optimisation in harvest robots. Biosystems Engineering, 2019; 183: 26–46.

[8] Marinoudi V, Sørensen C G, Pearson S, Bochtis D. Robotics and labour in agriculture. A context consideration. Biosystems Engineering, 2019; 184: 111–121.

[9] Johnson P C, Clementson C L, Mathanker S K, Grift T E, Hansen A C. Cutting energy characteristics of Miscanthus x giganteus stems with varying oblique angle and cutting speed. Biosystems Engineering, 2012; 112(1): 42–48.

[10] Wang Z H, Xun Y, Wang Y K, Yang Q H. Review of smart robots for fruit and vegetable picking in agriculture. Int J Agric & Biol Eng, 2022; 15(1): 33–54.

[11] Liu J, Peng Y, Faheem M. Experimental and theoretical analysis of fruit plucking patterns for robotic tomato harvesting. Computers and Electronics in Agriculture, 2020; 173: 105330.

[12] Matin M A, Fielke J M, Desbiolles J M A. Torque and energy characteristics for strip-tillage cultivation when cutting furrows using three designs of rotary blade. Biosystems Engineering, 2015; 129: 329–340.

[13] Yin J J, Chen Y H, He K, Liu J Z. Design and experiment of grape-picking device with grasping and rotary-cut type of underactuated double fingered hand. Transactions of the CSAM, 2017; 48(11): 12–20.

[14] Xu L M, Liu X D, Zhang K L, Xing J J, Yuan Q C, Chen J W, et al. Design

and test of end-effector for navel orange picking robot. Transactions of the CSAE, 2018; 34(12): 53–61.
[15] Ge Y, Zhang L X, Qian Y, Jiao X P, Chen Y B. Dynamic model for sucking process of pneumatic cutting-type safflower harvest device. Int J Agric & Biol Eng, 2016; 9(5): 43–50.
[16] Pathare P B, Baş N, Fitzpatrick J J, Cronin K, Byrne E P. Effect of high shear granulation process parameters on the production of granola cereal aggregates. Biosystems Engineering, 2011; 110(4): 473–481.
[17] Xiong Y, Ge Y, Grimstad L, From P J. An autonomous strawberry‐harvesting robot: Design, development, integration, and field evaluation. Journal of Field Robotics, 2020; 37(2): 202–224.
[18] Park Y, Seol J, Pak J, Jo Y, Kim C, Son H I. Human-centered approach for an efficient cucumber harvesting robot system: Harvest ordering, visual servoing, and end-effector. Computers and Electronics in Agriculture, 2023; 212: 108116.
[19] Wang Y, Yang Y, Zhao H, Liu B, Ma J T, He Y, Zhang Y T, Xu H B. Effects of cutting parameters on cutting of citrus fruit stems. Biosystems Engineering, 2020; 193: 1–11.
[20] Gracia L, Perez-Vidal C, Gracia-López C. Automated cutting system to obtain the stigmas of the saffron flower. Biosystems Engineering, 2009; 104(1): 8–17.
[21] Manuello Bertetto A, Ricciu R, Badas M G. A mechanical saffron flower harvesting system. Meccanica, 2014; 49: 2785–2796.
[22] Cao W B, Lian D G, Niu C, An L L, Yang S P, Chen B B. Harvest performance test and parameter optimization of comb-type safflower-filaments picking head at same height. Transactions of the CSAE, 2018; 34(22): 36–44.
[23] Zhang Z G, Xing Z Y, Yang S P, Feng N, Liang R Q, Zhao M Y. Design and experiments of the circular arc progressive type harvester for the safflower filaments. Transactions of the CSAE, 2022; 38(17): 10–21.
[24] Yan D, Luo L, Zhang P, Liu W, Wang J, Lu Q, Luo S. Vibration analysis and experimental study of the effects of mechanised grape picking on the fruit–stem system. Biosystems Engineering, 2023; 227: 82–94.
[25] Castro-Garcia S, Sola-Guirado R R, Gil-Ribes J A. Vibration analysis of the fruit detachment process in late-season 'Valencia'orange with canopy shaker technology. Biosystems Engineering, 2018; 170: 130–137.
[26] Van Herck L, Kurtser P, Wittemans L, Edan Y. Crop design for improved robotic harvesting: A case study of sweet pepper harvesting. Biosystems Engineering, 2020; 192: 294–308.
[27] Van Henten E J, Schenk E J, Van Willigenburg L G, Meuleman J, Barreiro P. Collision-free inverse kinematics of the redundant seven-link manipulator used in a cucumber picking robot. Biosystems Engineering, 2010; 106(2): 112–124.
[28] Zhou K H, Xia L R, Liu J, Qian M Y, Pi J. Design of a flexible end-effector based on characteristics of tomatoes. Int J Agric & Biol Eng, 2022; 15(2): 13–24.
[29] Gao J, Zhang F, Zhang J, Yuan T, Yin J, Guo H, Yang C. Development and evaluation of a pneumatic finger-like end-effector for cherry tomato harvesting robot in greenhouse. Computers and Electronics in Agriculture, 2022; 197: 106879.
[30] Carrasco E V, Smits M A, Alves R C, Pizzol V D, Oliveira A L, Mantilla J N. GluBam beams: Influence of the roughness of the bamboo laminas on the shear stress and the sliding modulus of bonded joint. Biosystems Engineering, 2021; 203: 98–108.
[31] Ucgul M, Saunders C. Simulation of tillage forces and furrow profile during soil-mouldboard plough interaction using discrete element modelling. Biosystems Engineering, 2020; 190: 58–70.
[32] Zhao X, Xu G J, Zhang P F, Yu G H, Xu Y D. Design and experimental study of the end-effector for broccoli harvesting. Int J Agric & Biol Eng, 2024; 17(1): 137–144.
[33] Li Y, Liu C. A log-spiral limit equilibrium analysis for passive earth pressure under the effect of unsaturated seepage conditions. European Journal of Environmental and Civil Engineering, 2023; 27(1): 374–392.
[34] Kudzaev A B. Comparison of different blade shapes of translatory moving soil tillage tools. Tractors and Agricultural Machinery, 2023; 90(4): 337–349.
[35] Xie L, Wang P, Luo J, Yi W, Deng J. Optimisation and numerical simulation of shearing blade used for citrus seedling grafting. Biosystems Engineering, 2022; 215: 67–79.
[36] Mousaviraad M, Tekeste M Z. Effect of grain moisture content on physical, mechanical, and bulk dynamic behaviour of maize. Biosystems Engineering, 2020; 195: 186–197.
[37] Vu V D, Ngo Q H, Nguyen T T, Nguyen H C, Nguyen Q T, Nguyen V D. Multi-objective optimisation of cutting force and cutting power in chopping agricultural residues. Biosystems Engineering, 2020; 191: 107–115.
[38] Mathanker S K, Grift T E, Hansen A C. Effect of blade oblique angle and cutting speed on cutting energy for energycane stems. Biosystems Engineering, 2015; 133: 64–70.
[39] Zhang Z G, Zhao M Y, Xing Z Y, Liu X F. Design and test of double-acting opposite direction cutting end effector for safflower harvester. Transactions of the CSAM, 2022; 53(12): 160–170.
[40] Song S, Zhou H, Jia Z, Xu L, Zhang C, Shi M, Hu G. Effects of cutting parameters on the ultimate shear stress and specific cutting energy of sisal leaves. Biosystems Engineering, 2022; 218: 189–199.
[41] Kuroyanagi T. Investigating air leakage and wind pressure coefficients of single-span plastic greenhouses using computational fluid dynamics. Biosystems Engineering, 2017; 163: 15–27.
[42] Giahi M, Bergstrom D J, Singh B. Computational fluid dynamics analysis of an agricultural spray in a crossflow. Biosystems Engineering, 2023; 230: 329–343.
[43] Sinha R, Ranjan R, Khot L R, Hoheisel G A, Grieshop M J. Drift potential from a solid set canopy delivery system and an axial–fan air–assisted sprayer during applications in grapevines. Biosystems Engineering, 2019; 188: 207–216.
[44] Yan C, Niu C, Ma S, Tan H, Xu L. CFD models as a tool to analyze the deformation behavior of grape leaves under an air-assisted sprayer. Computers and Electronics in Agriculture, 2022; 198: 107112.
[45] Gebrehiwot M G, De Baerdemaeker J, Baelmans M. Effect of a cross-flow opening on the performance of a centrifugal fan in a combine harvester: Computational and experimental study. Biosystems Engineering, 2010; 105(2): 247–256.
[46] Cao W B, Yang S P, Li S F, Jiao H B, Lian G D, Niu C, et al. Parameter optimization of height limiting device for comb-type safflower harvesting machine. Transactions of the CSAE, 2019; 35: 48–56.
[47] Du X, Liu C. Design and testing of the filling-plate of inner-filling positive pressure high-speed seed-metering device for maize. Biosystems Engineering, 2023; 228: 1–17.
[48] Gao X, Xie G, Li J, Shi G, Lai Q, Huang Y. Design and validation of a centrifugal variable-diameter pneumatic high-speed precision seed-metering device for maize. Biosystems Engineering, 2023; 227: 161–181.
[49] Xu J, Sun S, He Z, Wang X, Zeng Z, Li J, Wu W. Design and optimisation of seed-metering plate of air-suction vegetable seed-metering device based on DEM-CFD. Biosystems Engineering, 2023; 230: 277–300.
[50] Hołownicki R, Doruchowski G, Świechowski W, Godyń A, Konopacki P J. Variable air assistance system for orchard sprayers; concept, design and preliminary testing. Biosystems Engineering, 2017; 163: 134–149.
[51] Yang K, Yu Z, Luo W, Fan J, Li Y, Gu F, et al. Experiment and Study of Garlic Root Cutting Based on Continuous Force Feedback. Agronomy, 2023; 13(3): 835.
[52] Yang H, Chen L, Ma Z, Chen M, Zhong Y, Deng F, Li M. Computer vision-based high-quality tea automatic plucking robot using Delta parallel manipulator. Computers and Electronics in Agriculture, 2021; 181: 105946.
[53] Majeed Y, Zhang J, Zhang X, Fu L, Karkee M, Zhang Q, et al. Deep learning based segmentation for automated training of apple trees on trellis wires. Computers and Electronics in Agriculture, 2020; 170: 105277.
[54] Xing Z Y, Zhang Z G, Shi R M, Guo Q F, Zeng C. Filament-necking localization method via combining improved PSO with rotated rectangle algorithm for safflower-picking robots. Computers and Electronics in Agriculture, 2023; 215: 108464.